# 行政院國家科學委員會專題研究計畫 成果報告

## 用以提高發光二極體效率之表面電漿波研究
## 研究成果報告(精簡版)

計 畫 類 別 ：個別型
計 畫 編 號 ：NSC 95-2221-E-002-286-
執 行 期 間 ：95 年 08 月 01 日至 96 年 09 月 30 日
執 行 單 位 ：國立臺灣大學光電工程學研究所

計 畫 主 持 人：江衍偉

計畫參與人員：博士班研究生-兼任助理：王志洋
碩士班研究生-兼任助理：李明憲、郭嘉志、林俊安、莊文宏

公 開 資 訊 ：本計畫可公開查詢

中 華 民 國 96 年 10 月 26 日

# 行政院國家科學委員會專題研究計畫成果報告

## 用以提高發光二極體效率之表面電漿波研究

## Study of surface plasma waves for enhancing the efficiency of LEDs

**摘要：**

本報告中我們提出一基於邊界積分方程法之新穎數值技巧，用以探討二維週期結構之表面電漿波行為。針對問題中的週期性特點，我們採平面波展開法與週期性邊界條件，而不用週期性格林函數。一旦求解出等效表面電流與磁流，毋須作輻射積分，繞射效率便可輕易計算而得。藉計算高導電性材質與實際金屬材質之光柵問題，本數值方法之準確性亦得到驗證。即使入射角高達 80 度，本法之收斂性仍佳。我們以此數值方法計算波浪狀金屬-介質層狀結構。適當設計的結構可提升光波之穿透率。數值模擬顯示此種高穿透率係因激發表面電漿波所致。

**關鍵詞**：數值模擬、光柵、表面電漿波

**Abstract:** A novel hybrid technique based on the boundary integral-equation method is proposed for studying the surface plasmon polariton behaviors in two-dimensional periodic structures. Considering the periodicity property of the problem, we use the plane-wave expansion concept and the periodic boundary condition instead of using the periodic Green's function. The diffraction efficiency can then be readily calculated once the equivalent electric and magnetic currents are solved that avoids invoking the numerical calculation of the radiation integral. The numerical validity is verified with the cases of highly conducting materials and practical metals. Numerical convergence can be easily achieved even in the case of a large incident angle as $80^{o}$. Based on the numerical scheme, a metal-dielectric wavy structure is designed for enhancing the transmittance of optical signal through the structure. The excitation of the surface plasmon polariton for the high transmission is demonstrated.

**Keywords:** Numerical simulation, Gratings, Surface plasmons

### 1. Introduction

In recent years, the research of surface plasmon polaritons (SPPs) [1] in the near-infrared and visible ranges has received much attention since the phenomenon of SPP-mediated extraordinary transmission was discovered [2]. For theoretically investigating the SPP-related phenomena and designing the nanostructures for relevant applications, effective numerical methods are needed. Several numerical methods have been widely used for these purposes, including the finite-difference time-domain (FDTD) method [3], the finite-element method (FEM) [4], the integral equation method (IEM) [5-7], and the coupled-wave method (CWM) [8]. Among them, because of its computation efficiency for certain simple structures and simplicities in formulation and programming, the CWM is commonly used for calculating the diffraction efficiency of a periodic structure. However, the CWM suffers from inducing spurious features of diffraction efficiency in dealing with the structures of highly conducting materials [9, 10]. Another problem of slow convergence related to the staircase approximation for arbitrary-shaped metallic gratings is also encountered by the CWM [11].

In many SPP applications, the fine geometries of the structures are not in simple rectangular shapes and are usually quite complicated. In such a situation, the unstructured-mesh method is needed to precisely describe the problem geometry. The FEM and the IEM

are the possible choices. However, in this research, we choose the boundary integral-equation method (BIEM) because it is based on a surface formulation, which automatically takes care of the discontinuities between different materials [5]. Besides, all the unknowns in the formulation are designated only on the structure boundaries and interfaces. These features result in a smaller number of unknowns when compared with other unstructured-mesh numerical techniques based on volumetric formulations, such as the FEM or the volume IEM, in which the unknowns are designated in the bulky domain. To deal with the periodicity property in a periodic problem based on the BIEM, one can usually apply the periodic Green's function to the integral equation. However, the periodic Green's function is usually in a form of infinite series and thus may suffer from the problem of slow convergence. Although certain techniques have been developed for speeding up the convergence, the mathematical treatment and programming implementation in applying these techniques to the IEM are quite complicated and case-dependent [12,13]. Recently, a scheme of the BIEM was proposed, in which the periodic boundary condition was used and the free-space Green's function was utilized in the major part of the unit cells [6]. However, the concept of the periodic Green's function was still needed for the rest part of unit cells of homogeneous materials.

In this research, we develop a novel hybrid technique combining the BIEM with the plane-wave expansion method. This technique has the advantage of retaining the flexibility of the BIEM in solving a problem of complex geometry. It also takes the advantage of using the plane-wave expansion method to express the fields in the homogeneous regions such as those outside the wave coupling area of major concern. In addition, the expansion coefficients can be connected to the equivalent electric and magnetic surface currents, which are the unknowns to be solved in the BIEM. Thus, we can apply the periodic boundary condition in the direction of periodicity and truncate the computation domain in the perpendicular direction. Such a choice can help in avoiding using the periodic Green's function. The formulation can be applied to both metal and dielectric materials. Another advantage of this method is that the diffraction efficiency of any order can be directly calculated once the equivalent surface currents are solved such that the numerical calculation of the radiation integral is unnecessary.

This paper is organized as follows. In section 2, the formulation of the plane-wave-assisted BIEM is presented. The numerical verifications for the proposed method and the simulations on a metal-dielectric wavy structure are shown in section 3. Finally, conclusions are drawn in section 4.

## 2. Plane-wave-assisted boundary integral-equation method

In this research, we consider only the two-dimensional (2D) transverse electric (TE or p-wave) case, in which all quantities are independent of $z$. We assume that the electric field is polarized in the $x$-$y$ plane and the magnetic field is along the $z$ direction. The transverse magnetic (TM) case can be similarly treated. Before discussing the plane-wave-assisted method, let us recall the basic concept of the BIEM. The BIEM is based on the Stratton-Chu formulas [14, 15], which state that the total field at an observation point, $\vec{\rho}$, in an enclosed homogeneous, ($\varepsilon$, $\mu$), region can be calculated, in addition to the incident field, $(\vec{E}_{inc}, \vec{H}_{inc})$, by integrating all the contributions from the equivalent electric and magnetic surface currents, $(\vec{J}, \vec{M})$, on all boundaries of this region. If the observation point is located on a boundary (approaching from the interior of the region), the electric and magnetic fields in the 2D TE case can be expressed as

$$\begin{cases} \vec{E}(\vec{\rho}) = 2\vec{E}_{inc}(\vec{\rho}) \\ \quad +2\int\left\{ i\omega\mu\vec{J}(\vec{\rho}')\varphi(\vec{\rho},\vec{\rho}') - \vec{M}(\vec{\rho}')\times\nabla'\varphi(\vec{\rho},\vec{\rho}') - \left[\frac{i}{\omega\varepsilon}\nabla'\cdot\vec{J}(\vec{\rho}')\right]\nabla'\varphi(\vec{\rho},\vec{\rho}')\right\} dl' \\ \vec{H}(\vec{\rho}) = 2\vec{H}_{inc}(\vec{\rho}) \\ \quad +2\int\left[ i\omega\varepsilon\vec{M}(\vec{\rho}')\varphi(\vec{\rho},\vec{\rho}') + \vec{J}(\vec{\rho}')\times\nabla'\varphi(\vec{\rho},\vec{\rho}')\right] dl' \end{cases} . \quad (1)$$

Here, the line integrals are evaluated as the Cauchy principal values, and $\varphi(\vec{\rho},\vec{\rho}')$ is the 2D Green's function of the homogeneous region given by:

$$\varphi(\vec{\rho},\vec{\rho}') = \frac{i}{4}H_0^{(1)}\left(k\left|\vec{\rho}-\vec{\rho}'\right|\right). \quad (2)$$

Here, $H_0^{(1)}$ is the first-kind Hankel function of order zero, $\omega$ is the angular frequency, and $k = \omega(\mu\varepsilon)^{1/2}$. Once we have the field expressions on each interface approaching from different regions expressed by Eq. (1), we can match them to obtain a set of boundary integral equations.

Based on the BIEM, the concept of the plane-wave-assisted method is proposed and the formulation details are discussed in the following: As shown schematically in Fig. 1, a unit cell of a periodic structure repeats itself in the $x$ direction and extends infinitely its background materials ($\varepsilon_1$, $\mu_1$) and ($\varepsilon_3$, $\mu_3$) in the -$y$ and +$y$ directions, respectively. Region 2 contains a homogeneous material ($\varepsilon_2$, $\mu_2$), which can be a metal or dielectric. In addition to the solid lines describing the real structure boundaries, we introduce virtual boundaries as plotted in red dashed lines ($C_1$, $C_2$,..., $C_6$) for enclosing the major part of the unit cell. We define the region enclosed by these red dashed lines as the interior region. In contrast, the exterior region is defined as the rest part of the unit cell.

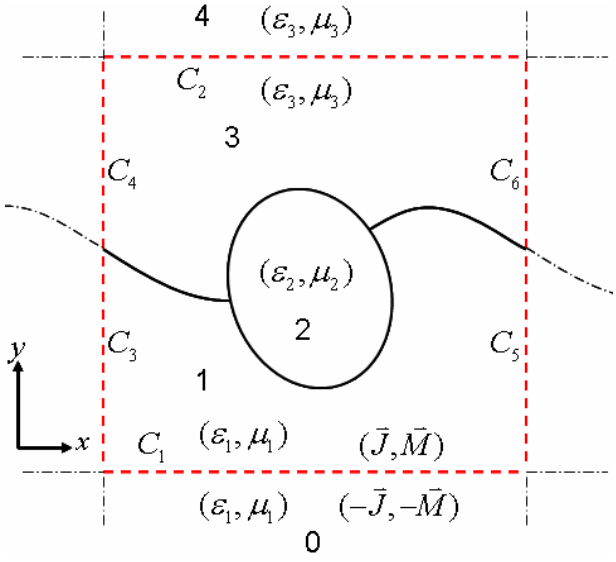


Fig. 1 A unit cell of a 2-D periodic structure. The unit cell repeats itself in the $x$ direction, with the solid lines for its true boundaries or interfaces. The red dashed lines represent virtual boundaries for applying the periodic boundary conditions and the interior-exterior connection.

On the virtual boundaries $C_3$-$C_4$ and $C_5$-$C_6$, the periodic boundary conditions are used. The fields on these boundaries in the interior region are related to each other through the Bloch condition. As to the field matching on the virtual boundaries $C_1$ and $C_2$, we develop a novel method based on the plane-wave expansion technique, which describes the field characteristics in the $y$-direction and provides a connection between the unknown coefficients of the expanded plane waves and those of the equivalent surface currents on the interior-exterior interfaces, ($C_1$ and $C_2$).

In Fig. 2, we show an alternative version of Fig. 1 to focus on the discussions of the interior-exterior interfaces.

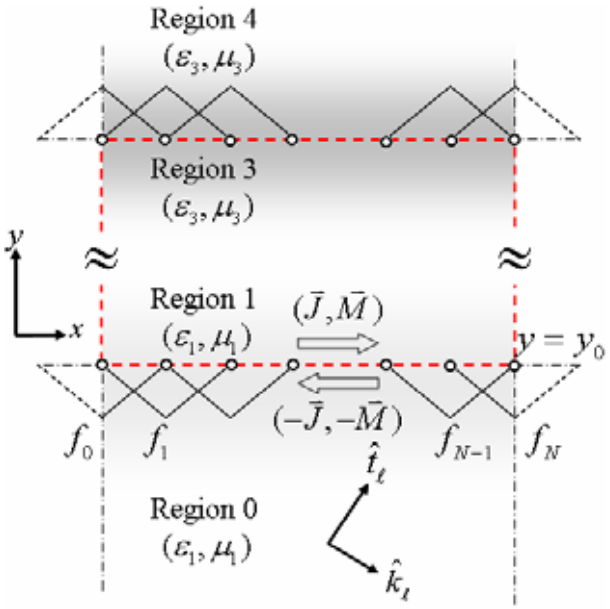


Fig. 2 An alternative version of Fig. 1 to focus on the discussions of the interior-exterior interfaces.

In region 0, a plane wave with transverse wavevector $k_x$ is incident onto the interior region, producing the reflected wave. The total electromagnetic field includes both the incident and reflected parts, which can be expanded with a set of plane waves in the Bloch form as

$$\begin{cases} \vec{E} = \vec{E}_{inc} + \vec{E}_{ref} = \vec{E}_{inc}(x,y) + \sum_{\ell=-L}^{L} \hat{t}_\ell \eta h_\ell e^{i(k_x+\ell G)x} e^{-ik_y^\ell (y-y_0)} \\ \vec{H} = \vec{H}_{inc} + \vec{H}_{ref} = \hat{z} H_{inc}(x,y) + \sum_{\ell=-L}^{L} \hat{z} h_\ell e^{i(k_x+\ell G)x} e^{-ik_y^\ell (y-y_0)} \\ k_y^\ell = \sqrt{k^2 - (k_x+\ell G)^2}, \ \ \mathrm{Re}(k_y^\ell) \ge 0, \ \ \mathrm{Im}(k_y^\ell) \ge 0 \end{cases} . \tag{3}$$

Here, $\eta$ is the intrinsic impedance of the background material, $h_\ell$ is the coefficient to be solved, and $G$ is the primitive translation wavevector of the 1D grating with period $a$. The incident wave can be in any form satisfying the Bloch condition. Here we define a vector $\hat{t}_\ell = \hat{z} \times \hat{k}_\ell$ for describing any order of the reflected electric field with

$$\hat{k}_\ell = \hat{x} \frac{(k_x + \ell G)}{k} - \hat{y} \frac{k_y^\ell}{k} .$$

As to the connection of the plane-wave expansion coefficients, $h_\ell$, in Eq. (3) and the unknown equivalent surface current, $\bar{J}$, at the interface $y = y_0$ between regions 0 and 1, we consider the following equation for $\bar{J}$ as

$$\begin{cases} \vec{J}(x) = \sum_{n=0}^{N} \hat{x} J_n f_n(x), \quad N = 2L+1 \\ -\vec{J}(x) = (-\hat{y}) \times \vec{H}(x, y_0) \end{cases}. \tag{4}$$

Here, at the interface $y = y_0$, the tangential component of the total magnetic field is related to the equivalent electric surface current through a set of local linear bases $f_n = f_{n,1} + f_{n,2}$ given by

$$f_{n,1} = \begin{cases} \dfrac{x - x_{n-1}}{x_n - x_{n-1}}, & x_{n-1} \le x \le x_n \\ 0, & \text{otherwise} \end{cases}, \quad f_{n,2} = \begin{cases} \dfrac{x_{n+1} - x}{x_{n+1} - x_n}, & x_n \le x \le x_{n+1} \\ 0, & \text{otherwise} \end{cases}. \tag{5}$$

At a discretization point $x_n$, we have

$$\sum_{n'=0}^{N} \hat{x} J_{n'} f_{n'}(x_n) = \hat{y} \times \left[ \hat{z} H_{inc}(x_n, y_0) + \sum_{\ell=-L}^{L} \hat{z} h_\ell e^{i(k_x + \ell G) x_n} \right]. \tag{6}$$

Here, we consider the matching condition only at the sampled points $x_0$, $x_1$, …, $x_{N-1}$, because they can provide the variations of fields or currents in one period. Thus, the transformation between the coefficients of the local linear bases and those of the global plane waves can be easily obtained as

$$\begin{cases} J_n = H_{inc}(x_n, y_0) + \sum_{\ell=-L}^{L} P_{n\ell} h_\ell \\ h_\ell = \sum_{n=0}^{N-1} \left[ Q_{\ell n} J_n - Q_{\ell n} H_{inc}(x_n, y_0) \right] \end{cases}, \tag{7}$$

where $P_{n\ell} = e^{i(k_x + \ell G) x_n}$, and $Q_{\ell n}$ are the elements of the inverse of the matrix $[P_{n\ell}]$. In our simulations, the condition number of $[P_{n\ell}]$ is close to unity that guarantees the numerical stability.

Based on Eqs. (3) and (7), we can express the total electromagnetic field in region 0 in terms of the coefficients of the equivalent electric surface current $J_n$ as

$$\begin{cases} \vec{E} = \vec{E}_{inc}(x, y) + \sum_{\ell=-L}^{L} \sum_{n=0}^{N-1} \hat{t}_\ell \eta \left[ Q_{\ell n} J_n - Q_{\ell n} H_{inc}(x_n, y_0) \right] e^{i(k_x + \ell G) x} e^{-i k_y^\ell (y - y_0)} \\ \vec{H} = \hat{z} H_{inc}(x, y) + \sum_{\ell=-L}^{L} \sum_{n=0}^{N-1} \hat{z} \left[ Q_{\ell n} J_n - Q_{\ell n} H_{inc}(x_n, y_0) \right] e^{i(k_x + \ell G) x} e^{-i k_y^\ell (y - y_0)} \end{cases}. \tag{8}$$

Note that Eq. (8) not only describes the field property in the exterior region of reflection (region 0), but also provides a connection to the fields in the interior region (region 1). The field expressions in the exterior region of transmission (region 4) can also be derived in a similar way without the contribution of the incident field.

When expanding the equivalent surface current on boundary $C_1$ using the linear bases, care must be taken. For the bases $f_n$ plotted in Fig. 2, $f_0$ contains only $f_{0,2}$, while $f_N$ contains only $f_{N,1}$. Note that $J_N = J_0 e^{ik_x a}$ based on the Bloch condition.

With Eq. (8), we can match the boundary condition on $C_1$ to obtain an integral equation, which contains only the unknown coefficients of the equivalent currents of the interior region. After matching the boundary conditions on all boundaries or interfaces of the interior region, we use the Galerkin testing procedure to transfer the whole integral equation into a matrix equation. The entire matrix equation can be expressed in the form of

$$\begin{bmatrix} \mathbf{A} & \mathbf{B} \\ \mathbf{C} & \mathbf{D} \end{bmatrix} \begin{bmatrix} \mathbf{J} \\ \mathbf{M} \end{bmatrix} = \begin{bmatrix} \mathbf{b}_E \\ \mathbf{b}_H \end{bmatrix}. \tag{9}$$

Here, **A**, **B**, **C**, and **D** are coefficient matrices with their elements obtained by calculating a double integral over the domains of two basis functions. Also, **J** and **M** are column vectors formed with the unknown coefficients of the equivalent surface currents, $\vec{J}$ and $\vec{M}$, respectively. The incident fields, $\vec{E}_{inc}$ and $\vec{H}_{inc}$, are tested with the testing procedure to form the two column vectors, $\mathbf{b}_E$ and $\mathbf{b}_H$, respectively.

Certain matrix elements formed in testing the fields of Eq. (8) are in the form of

$$\sum_{\ell=-L}^{L} \sum_{n=0}^{N-1} c_{\ell n} \int f_n(x) e^{i(k_x + \ell G)x} dx \,. \tag{10}$$

Such an integration may be quite time consuming in computation. However, the integration with the factor $f_n(x)e^{i(k_x+\ell G)x}$ can be analytically calculated. Also, it is only related to the outer summation in Eq. (10). These features remarkably save the computation time. Note also that once the equivalent surface currents are obtained through matrix inversion, the reflected and transmitted fields of any diffraction order in the exterior region can be readily calculated with Eq. (3) without numerical calculation of the radiation integral. This is one of the advantages of our method.

## 3. Simulation results

### *3. A. Numerical verifications*

To verify the numerical accuracy of the proposed method, we first consider a reflection-type highly-conducting metallic-lamellar grating with the dielectric constant $\varepsilon_\gamma$ = -100 ($n = i10$), as depicted in Fig. 3.

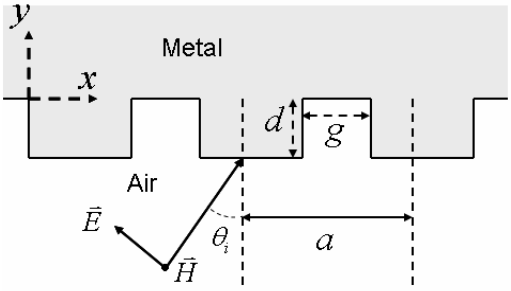


Fig. 3 A reflection-type metallic-lamellar grating with a grating period *a*, a groove depth *d*, and a groove width *g*. The incident wave is p-polarized with an incident angle $\theta_i$.

The numerical convergence in the calculation of diffraction efficiency of a highly-conducting lamellar grating has been a widely studied issue associated with the CWM, which is based on the concept of plane-wave expansion. In Fig. 4(a), we show the reflectance of the -1 order versus the groove width based on the CWM with the same parameters used in [9]. Both the period *a* and the groove depth *d* are set to be 500 nm. The groove width *g* is taken to be a varying parameter from 5 to 460 nm. The incident field is TE- or p-polarized with the wavelength $\lambda_0$ = 632.8 nm and the incidence angle $\theta_i = 30^o$. Quite many sharp reflectance peaks and dips can be seen in Fig. 4(a), which have been proved spurious and are not the real physical features, even though we have used Li's Fourier factorization in our calculation [16]. For comparison, Fig. 4(b) shows the result calculated with the proposed method. Here, one can see that the major reflectance variation curve is almost the same as that in Fig. 4(a). The

major difference is that those spurious features in Fig. 4(a) disappear. Our result also matches well with that calculated with the rigorous modal method [9]. The superiority of the proposed method to the CWM in this application is due to the fact that we use the plane-wave expansion technique only in the homogeneous regions exterior to the grating region where the rapid field variation is carefully treated with the BIEM.

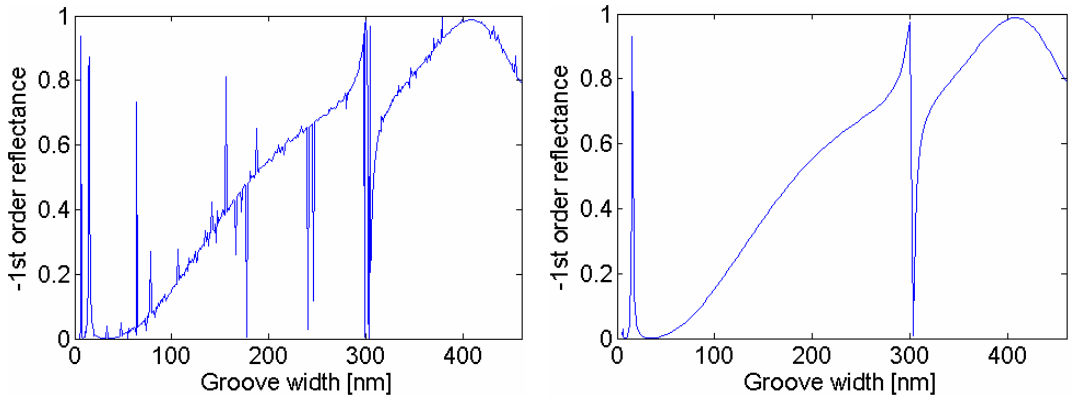


(a) (b)

Fig. 4 Reflectance of the -1 order versus the groove width, calculated with (a) the coupled-wave method (CWM) and with (b) the proposed method.

Another accuracy verification is shown in Fig. 5 with the same problem geometry shown in Fig. 3.

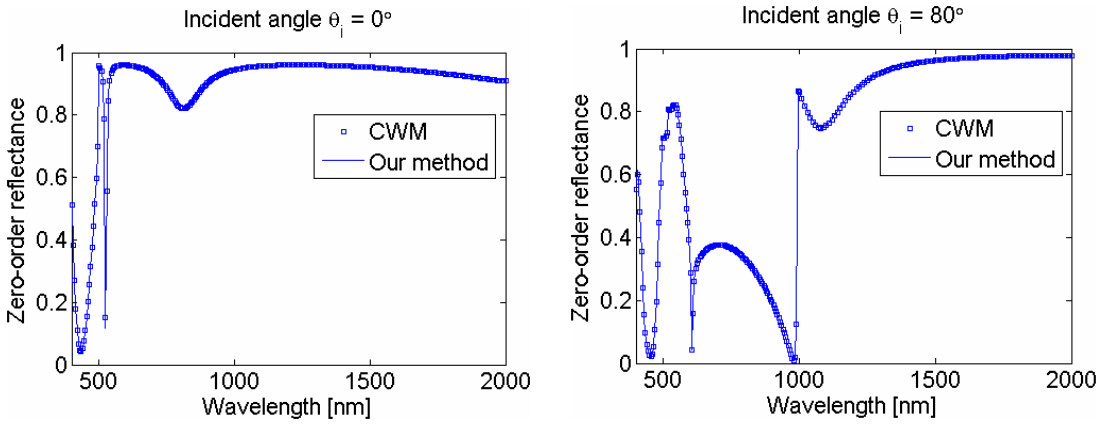


(a) (b)

Fig. 5 Zero-order reflectance versus wavelength. Solid lines denote the results of our method and empty squares represent those calculated with the CWM. (a) $\theta_i = 0^o$. (b) $\theta_i = 80^o$.

The groove width is fixed at 250 nm. The metal is changed into Ag, whose dielectric constant can be described by the Drude model $\varepsilon_r = 1 - \omega_p^2/[\omega(\omega + i\gamma_p)]$, with the plasma frequency $\omega_p$ = $1.36 \times 10^{16}$ $s^{-1}$ (corresponding to the energy of 9 eV) and the damping frequency $\gamma_p = \omega_p/90$. The result of the zero-order reflectance versus the wavelength of a normally incident wave is shown in Fig. 5(a). The solid line indicates the result calculated with the proposed method and the empty squares denote that with the CWM. They match almost perfectly with each other. We further take a large incident angle of $80^o$ for numerical verification with the result shown in Fig. 5(b). In this case, the proposed method also leads to almost exactly the same result as

that based on the CWM. Note that some other methods using the perfectly matched layer (PML) for truncating the computation domain in the perpendicular direction cannot lead to accurate results when the incident angle is large. In this situation, a lot of PML layers are needed and a large memory space for computing is required.

*3. B. Simulation results of a wavy structure*

After verifying the accuracy of the proposed method, we simulate a wavy layered structure with a substrate-metal-cover-air architecture. For numerical implementations, the substrate is assumed to be GaN (with the refractive index of 2.5), covered by Ag. The material of the dielectric cover has a refractive index $n_c$, which is left as a varying parameter. The geometry of the structure is shown in Fig. 6, where $a$ is the grating period, and $A$ is the amplitude of the sinusoidal variation. The thicknesses of the silver layer and the dielectric cover layer are denoted by $t_m$ and $t_c$, respectively. A wave is normally incident toward the $+y$ direction from the substrate.

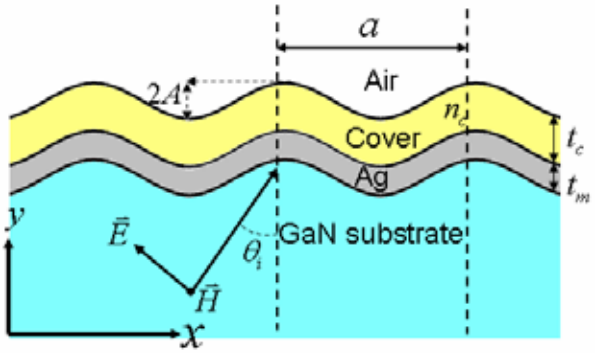


Fig. 6 Schematic illustration of a wavy layered structure. The grating period is $a$, and the amplitude of the sinusoidal variation is $A$. The cover layer, with its thickness denoted by $t_c$, has a refractive index $n_c$. The thickness of the Ag film is $t_m$.

With the problem geometry, we will examine the zero-order transmittance and power loss versus the wavelength of the incident light for different structure parameters. Here, the power loss is calculated by subtracting all the diffracted power from the incident power. First, a set of standard parameters is chosen as $a$ = 218 nm, $A$ = 20 nm, $t_m$ = 44 nm, $t_c$ = 100 nm, and $n_c$ = 2.5. We first assume that the cover has a refractive index the same as that of the GaN substrate and is thicker than the decay length of the SPP mode. Therefore, the problem geometry becomes symmetric. The assumption of 218 nm for the period $a$ means to excite an SPP mode at $\lambda_0$ = 650 nm according to the diffraction relation,

$$k_x = n\,(2\pi/a) + k_{\mathrm{SPP}}. \tag{11}$$

Here, $k_x$ is the in-plane wavevector of the incident wave, $k_{\mathrm{SPP}}$ is the wavevector of the SPP mode [1] at the planar Ag/GaN interface, and $n$ is an appropriate integer. The result from Eq. (11) is an estimate based on the assumptions that the corrugation just causes a small perturbation and the Ag film is thick enough such that the optical activities of its upper and lower interfaces can be regarded independent.

By taking the silver thickness $t_m$ as a varying parameter, changing from 44 to 28 nm, the transmittance and power loss versus wavelength are shown in Fig. 7. In Fig. 7(a), the transmittance peak location blue shifts as $t_m$ decreases. However, a shoulder is gradually formed on the long-wavelength side. The maximum peak reaches 0.78 at $t_m$ = 28 nm. At $t_m$ = 44 nm, the transmittance peak is located at 656 nm, which is close to the designed wavelength from Eq. (11). In Fig. 7(b), one can see a major and a minor peak in all the power loss spectra. The major loss peak presents a red-shift trend while the minor one shows an opposite trend in decreasing $t_m$. Comparing Figs. 7(a) and (b), one can see that the transmittance peak is always

close to the minor loss peak. Therefore, one can separate the transmittance peak and the major loss peak by narrowing down the Ag layer.

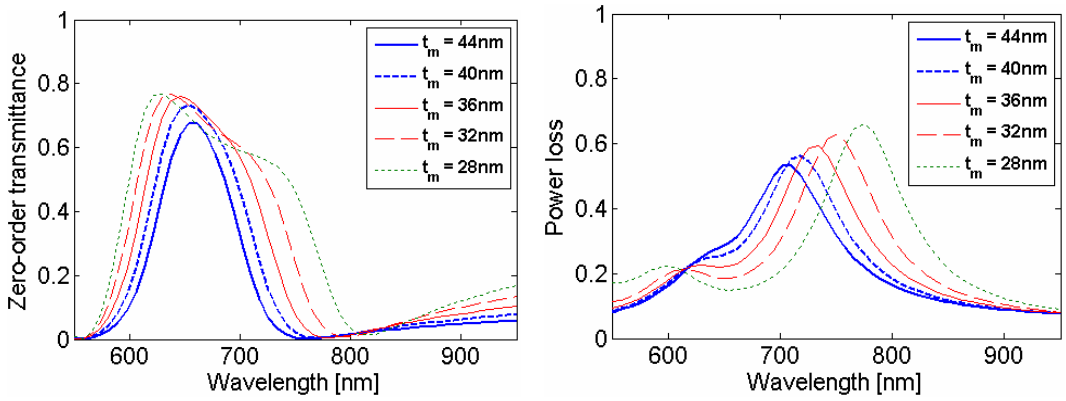


(a) (b)

Fig. 7 (a) Zero-order transmittance and (b) power loss versus wavelength. The results are calculated for different Ag-film thicknesses.

Then, we take the grating amplitude $A$ as a varying parameter, changing from 24 to 8 nm, to give Fig. 8, in which a slight blue shift of the transmittance peak in decreasing $A$ can be seen. The transmittance peak level reduces considerably when $A$ becomes smaller. The power loss variation shown in Fig. 8(b) reveals that the reduction of transmittance is mainly due to the metallic loss of the SPP modes, other than the reflection. One can again see that the transmittance peak is close to the minor loss peak in the loss spectrum.

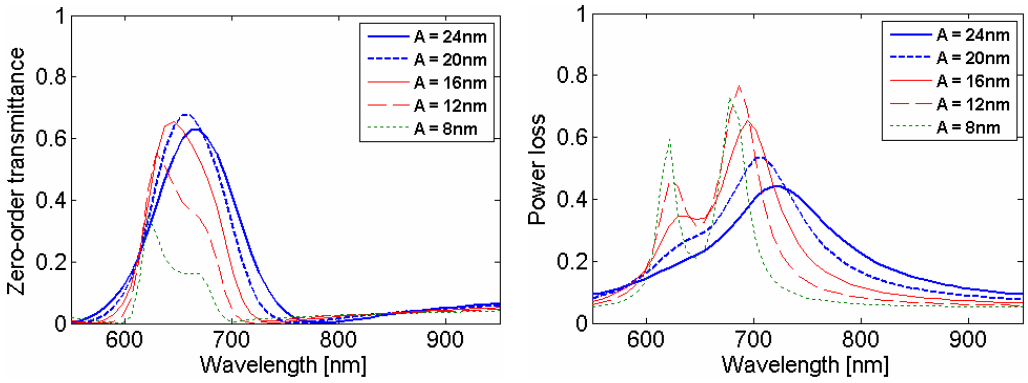


(a) (b)

Fig. 8 (a) Zero-order transmittance and (b) power loss versus wavelength. The results are calculated for different amplitudes of the sinusoidal shape.

Next, we change the refractive index of the cover layer $n_c$ from 2.5 into 2.7, with other parameters remaining the same with the aforementioned standard ones. Now, because the problem geometry becomes asymmetric, the designated grating period of 218 nm is no longer appropriate for inducing the SPP coupling at $\lambda_0$ = 650 nm. Therefore, compared with the result of the symmetric structure, a transmittance reduction and a red-shift trend are expected in this asymmetric case. In this case, we vary the cover layer thickness $t_c$ from 100 to 50 nm to see the effects on the transmittance and power loss. The numerical results are shown in Fig. 9. The transmittance peak in Fig. 9(a) is blue-shifted when $t_c$ is decreased. The peak level reaches a maximum at about 0.7 when $t_c$ = 70 nm and then decreases as $t_c$ becomes thinner. In Fig. 9(b), the major power loss peak is also blue-shifted with decreasing $t_c$.

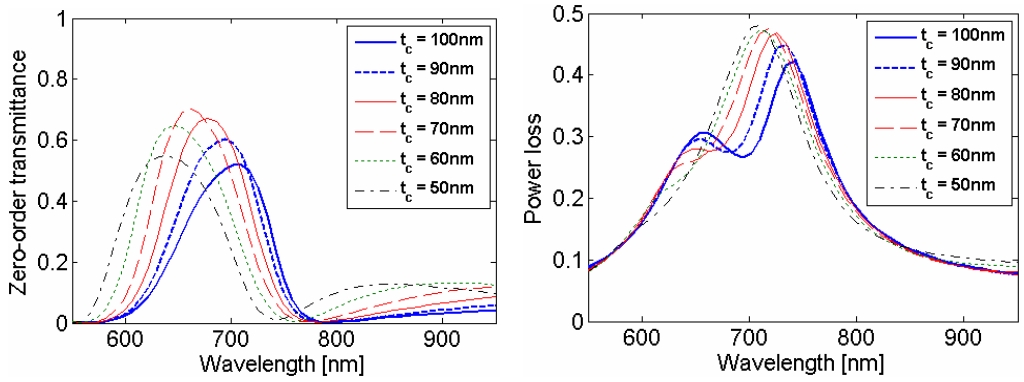


(a) (b)

Fig. 9 (a) Zero-order transmittance and (b) power loss versus wavelength. The results are calculated for different thicknesses of the cover layer.

With the asymmetric structure of $n_c$ = 2.7 and $a$ = 218 nm, we change other parameters into $A$ = 20 nm, $t_m$ = 28 nm, and $t_c$ = 70 nm, based on the results in Figs. (7)-(9) to optimize the transmittance level. The results are shown in Fig. 10.

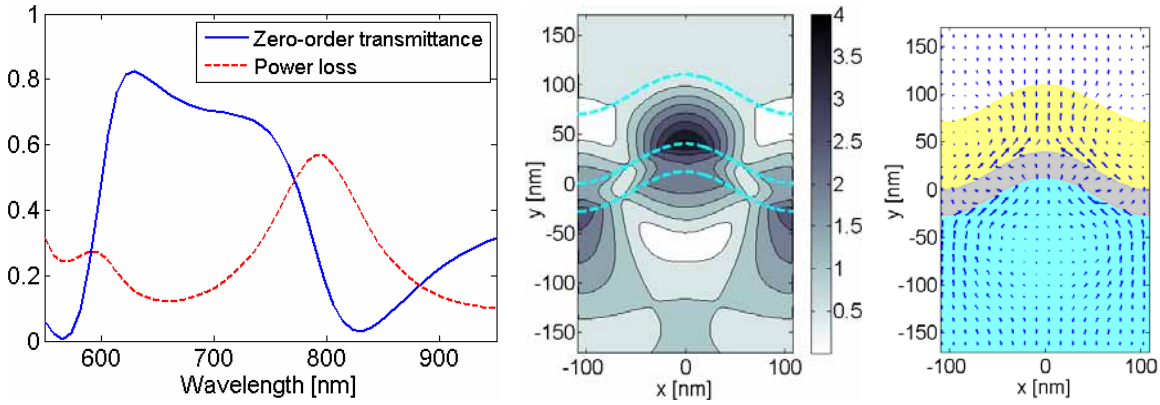


(a) (b) (c)

Fig. 10 (a) Zero-order transmittance and power loss versus wavelength. The structure parameters used are $a$ = 218 nm, $A$ = 20 nm, $t_m$ = 28 nm, $t_c$ = 70 nm, and $n_c$ = 2.7. (b) Distribution of the absolute value of the magnetic field at $\lambda_0$ = 630 nm. (c) Distribution of the time-average Poynting vector at $\lambda_0$ = 630 nm.

By adjusting the parameters, the transmittance shown in Fig. 10(a) becomes larger than 0.7 over a wide wavelength range from 610 to 700 nm. The transmittance peak value reaches 0.83 at 630 nm. Figure 10(b) shows the distribution of the absolute value of the magnetic field at the transmittance peak wavelength with the amplitude of the incident magnetic field set at unity. The localized field distributions on the two sides of the Ag film manifest an SPP feature, showing that the enhanced transmittance is due to the coupling of the SPP modes on the two sides. This result is different from the situation of a slit grating structure, in which transmittance is mainly enhanced by the cavity-mode component in the slits [17]. The distribution of the time-average Poynting vector illustrated in Fig. 10(c) also shows a result different from that in a slit grating structure. Here, the power flow is directly passing through the metal film via the SPP coupling. Though we use the sinusoidal shape as the grating geometry to demonstrate the capability of the proposed numerical method, similar results can be obtained in other sinusoid-like shapes. Based on our numerical studies, transmittance as high as 0.8 can be reached by adjusting the cover layer thickness as long as its refractive index is not much larger than that of the substrate.

## 4. Conclusions

We have developed a novel hybrid method, based on the BIEM and assisted with the plane-wave expansion technique. This method is flexible and applicable to various 2D grating structures, particularly those with metal/dielectric interfaces. Numerical accuracy has been verified with highly conducting and practical metals. This method can provide quite accurate results in the cases of large incidence angles. The transmittance of a metal/dielectric wavy structure has been investigated with various structure parameters. High transmittance up to 0.83 was obtained. The numerical results also showed that the transmittance enhancement was due to the coupling of the SPP modes on the two sides of the metal layer that was different from the situation of a slit grating structure.

## References


1. H. Raether, *Surface Plasmons* (Springer-Verlag, Berlin, 1988).
2. T. W. Ebbesen, H. J. Lezec, H. F. Ghaemi, T. Thio, and P. A. Wolff, "Extraordinary optical transmission through sub-wavelength hole arrays," Nature **391**, 667-669 (1998).
3. K. S. Yee, "Numerical solution of initial boundary value problems involving Maxwell's equations in isotropic media," IEEE Trans. Antennas Propagat. **14**, 302-307 (1966).
4. S. D. Gedney and R. Mittra, "Analysis of the electromagnetic scattering by thick gratings using a combined FEM/MM solution," IEEE Trans. Antennas Propagat. **39**, 1605-1614 (1991).
5. K. Yashiro and S. Ohkawa, "Boundary element method for electromagnetic scattering from cylinders," IEEE Trans. Antennas Propagat. **33**, 383-389 (1985).
6. L. C. Trintinalia and H. Ling, "Integral equation modeling of multilayered doubly-periodic lossy structures using periodic boundary condition and a connection scheme," IEEE Trans. Antennas Propagat. **52**, 2253-2261 (2004).
7. T. Sondergaard, S. I. Bozhevolnyi, and A. Boltasseva, "Theoretical analysis of ridge grating for long-range surface plasmon polaritons," Phys. Rev. B **73,** 045320 (2006).
8. M. G. Moharam and T. K. Gaylord, "Rigorous coupled-wave analysis of metallic surface-relief gratings," J. Opt. Soc. Am. A **3,** 1780-1796 (1986).
9. E. Popov, B. Chernov, M. Nevière, and N. Bonod, "Differential theory: Application to highly conducting gratings," J. Opt. Soc. Am. A **21**, 199-206 (2004).
10. K. Watanabe, "Study of the differential theory of lamellar gratings made of highly conducting materials," J. Opt. Soc. Am. A **23**, 69-72 (2006).
11. E. Popov, M. Nevie`re, B. Gralak, and G. Tayeb, "Staircase approximation validity for arbitrary-shaped gratings," J. Opt. Soc. Am. A **19**, 33-42 (2002).
12. K. Yasumoto and K. Yoshitomi, "Efficient calculation of lattice sums for free-space periodic Green's function," IEEE Trans. Antennas Propagat. **47**, 1050-1055 (1999).
13. H. Rogier and D. De Zutter, "A fast converging series expansion for the 2-d periodic Green's function based on perfectly matched layers," IEEE Trans. Microwave Theory Tech. **52**, 1199-1206 (2004).
14. J. A. Stratton, *Electromagnetic Theory* (McGraw-Hill, New York, 1941).
15. K.-M. Chen, "A mathematical formulation of the equivalence principle," IEEE Trans. Microwave Theory Tech. **37**, 1576-1581 (1989).
16. L. Li, "Use of Fourier series in the analysis of discontinuous periodic structures," J. Opt. Soc. Am. A **13**, 1870-1876 (1996).
17. D. Crouse and P. Keshavareddy, "Role of optical and surface plasmon modes in enhanced transmission and applications," Opt. Express **13**, 7760-7771 (2005).